RAA 2015 Vol. **15** No. **9**, 1571–1586 doi: 10.1088/1674–4527/15/9/013
http://www.raa-journal.org *http://www.iop.org/journals/raa*

Research in Astronomy and Astrophysics

Feasible region and stability analysis for hovering around elongated asteroids with low thrust

Hong-Wei Yang, Xiang-Yuan Zeng and Hexi Baoyin

School of Aerospace Engineering, Tsinghua University, Beijing 100084, China;
baoyin@tsinghua.edu.cn

Received 2014 September 22; accepted 2015 February 7

Abstract This paper investigates properties of low-thrust hovering, including the feasible region and stability, in terms of the dynamical parameters for elongated asteroids. An approximate rotating mass dipole model, by which the description of the rotational gravitational field is reduced to two independent parameters, is employed to construct normalized dynamical equations. The boundaries of the feasible region are determined by contours representing the magnitude of the active control. The effects of a rotating gravitational field and maximal magnitude of the low thrust on the feasible hovering regions are analyzed with numerical results. The stability conditions are derived according to the forms of the eigenvalues of the linearized equation near the hovering position. The stable regions are then determined by a grid search and the effects of the relevant parameters are analyzed in a parametric way. The results show that a close hovering can be easier to realize near the middle of the asteroid than near the two ends in the sense of both required control magnitude and stability.

Key words: space vehicles — celestial mechanics — cosmology — observations

1 INTRODUCTION

There is increasing interest in asteroid missions in many space agencies (e.g. NASA, JAXA, ESA, etc.). The NEAR Shoemaker mission was the first to land on a near-Earth asteroid (NEA) (Dunham et al. 2002). The Hayabusa mission successfully sampled the surface of an NEA (Itokawa) (Kawaguchi et al. 2008). The Dawn mission has been launched to explore the most two massive asteroids in the main belt, Vesta and Ceres (Russell & Raymond 2012). Recently, several sample return missions to NEAs have been proposed, including MarcoPolo-R (Barucci et al. 2012), OSIRIS-Rex (Lauretta & OSIRIS-Rex Team 2012) and Hayabusa2 (Tsuda et al. 2013). A variety of scientific and technological advancements are expected to be achieved in these missions such as investigating the formation of the early solar system (Barucci et al. 2012), characterization of potentially hazardous asteroids (Lauretta & OSIRIS-Rex Team 2012), asteroid cratering operations (Tsuda et al. 2013), etc. Moreover, CNSA's Chang'e-2 conducted a successful flyby of Toutatis which is a potentially hazardous asteroid (Hang et al. 2013). The transportation and origin of potentially hazardous asteroids have been previously investigated in the work of Ji & Liu (2007).

One effective way to explore an asteroid from a nearby perspective in its vicinity is body-fixed hovering, by which the spacecraft maintains its relative position with respect to the asteroid. Body-fixed hovering can be used to obtain high-resolution measurements of a target area on the asteroid's surface, and to simplify the descent and ascent maneuvers in a sample return mission (Broschart & Scheeres 2005). Such maneuvers were necessary in the Hayabusa mission (Scheeres 2004). A series of studies on hovering control methods has been published, including a tight control method using altimetry (Sawai et al. 2002), a dead band control (Broschart & Scheeres 2005) and a reinforcement learning method (Gaudet & Furfaro 2012), etc. These studies focus on the design and stability of a closed loop control system. However, the effects of the dynamical parameters on the hovering region and stability in the vicinity of an asteroid have not been analyzed. Jiang et al. (2014) analyzed body-fixed hovering at the natural equilibrium points (EPs) and classified the manifolds near the EPs into eight types, which depend on the gravity associated with the asteroid. The relationship between the physical parameters and the number of natural EPs has also been analyzed by numerical methods (Wang et al. 2014). No active control was assumed in these two studies so that a spacecraft can only hover at the natural EPs. The feasible hovering region where the gravitational force and the centrifugal force can be balanced by the external force can be enlarged with active control. Williams & Abate (2009) proposed solar sail body-fixed hovering and analyzed the effect of solar latitude and the sail area on the hovering region. Zeng et al. (2014a) analyzed hovering using non-ideal solar sails and complemented the work of Williams & Abate (2009). Compared with using a solar sail, a low thrust spacecraft has two main advantages. Firstly, the magnitude of the control is not limited by the direction of the control for low thrust, so it is easier to provide the desired control by applying low thrust. Secondly, the low thrust technique is mature and has been used in deep space missions, e.g., the Hayabusa mission (Kuninaka et al. 2007). Hence, it is interesting to study body-fixed hovering using low thrust.

In this paper, the feasible region and stability for body-fixed hovering in the vicinity of an elongated asteroid (such as (216) Kleopatra, (951) Gaspra, (1620) Geographos, etc.) using low thrust are studied. The effects of dynamical parameters, including the rotating gravitational field and the maximal magnitude of the active control provided by the low thrust, are analyzed. The gravity near an elongated asteroid is quite irregular. The traditional spherical harmonic expansion method is hard to converge (Scheeres et al. 2000). The polyhedral-shape modeling method proposed by Werner & Scheeres (1996) is an accurate method to model the gravitational field. However, this method is a numerical way which is based on different shape-data of asteroids. Hence, it is hard to use the polyhedral-shape modeling method to analyze the relationship between the hovering characteristics and dynamical properties. To investigate effects of the dynamical parameters on the characteristics of body-fixed hovering and obtain qualitative conclusions, an approximate and simplified model is preferred. Several simplified models have already been proposed for elongated asteroids, such as a massive straight segment (Riaguas et al. 1999), two perpendicular material segments (Bartczak & Breiter 2003), and a rotating mass dipole in which two point masses are connected with a massless rod (Prieto-Llanos & Gomez-Tierno 1994). The rotating mass dipole is employed in this paper due to the simplicity of its model formulation, where the rotating gravitational field of the asteroid can be characterized by only two dynamical parameters in its normalized form (Prieto-Llanos & Gomez-Tierno 1994; Zeng et al. 2014b). Recently, this approximate model has been developed to describe natural elongated asteroids whose model is established by the polyhedral-shape modeling method (Werner & Scheeres 1996) in the work of Zeng et al. (2014b). Essentially, this model can be regarded as a generalization of the circular restricted three body problem (CRTBP) (Prieto-Llanos & Gomez-Tierno 1994). Also, the body-fixed hovering position in the rotating mass dipole model can be regarded as a generalization of the artificial equilibrium points (AEPs) in the CRTBP (Morimoto et al. 2007). Abundant literatures have been published on AEPs and different kinds of active control have been studied including low thrust (Morimoto et al. 2007), solar sail (Baoyin & McInnes 2006) hybrid low-thrust propulsion (Baig & McInnes 2008), etc. In contrast to the CRTBP, the rotational velocity of the system is not only related the gravitational force and force between the two primaries but also the tensile force or compressive force acting on the massless rod in the rotating mass dipole model. Hence, the characteristics of body fixed hovering are not the same as those of the AEPs. The effects of these two dynamical parameters and the maximal magnitude of the active control on the feasible hovering region and stability will be analyzed by numerical methods in this paper. As for a spacecraft near an asteroid, it is affected by multiple perturbations, among which the solar radiation pressure may be the most important (Scheeres 2012). In the work of Scheeres (2012), the combined effects of the asteroid's gravity, solar gravity and solar radiation pressure on orbits around an asteroid are studied. Although there are many perturbations in addition to the asteroid's nonspherical perturbation, the work of Llanos et al. (2014) indicates that the magnitudes of the perturbations are quite small compared with the asteroid's gravity close to its surface (the ratio can be less than 0.001). Therefore, small perturbations from sources like the Sun and other planets are ignored in this paper.

The rest of this paper is organized as follows. Section 2 gives the dynamical equations using the simplified gravitational model and the condition for the ideal body-fixed hovering above an elongated asteroid. In Section 3, the feasible region in terms of the dynamical parameters are analyzed for both equatorial plane and out of equatorial plane. Also, magnitudes of the required control for several natural asteroids are evaluated in Section 3. Section 4 analyzes the stability in terms of the dynamical parameters. Section 5 concludes this paper.

2 DYNAMICAL EQUATIONS AND HOVERING FORMULATION

2.1 Dynamical Equations in a Body-fixed Frame

The problem of body-fixed hovering around an elongated asteroid is considered. The motion of a spacecraft in the vicinity of a natural asteroid depends on the physical properties of the asteroid, including its total mass, mass distribution, rotation period, etc. To analyze the characteristics of hovering around an elongated asteroid, a simple approximate model (i.e. a rotating mass dipole) is used for the rotating elongated asteroid (Prieto-Llanos & Gomez-Tierno 1994; Zeng et al. 2014b). Previous work has studied the connection between the rotating mass dipole and natural elongated bodies, showing that this model can be taken as a good approximation for natural asteroids (Zeng et al. 2014b). In this model, an asteroid is represented in a simplified way as two primary masses, m_1 and m_2, separated by a massless rod with a characteristic distance d, rotating around the combined center of mass M. A schematic diagram is shown in Figure 1. The synodic frame o-xyz centered at the center of mass is used as the body-fixed frame. The axis ox is collinear with the massless rod, the axis oz is aligned with the rotational angular velocity of the asteroid, and the axis oy completes the right handed coordinate system. The rotational angular velocity $\boldsymbol{\omega}$ of the synodic frame is assumed to be equal to the one of the asteroid. The synodic frame o-xyz is initially assumed to coincide with the inertial frame o-XYZ.

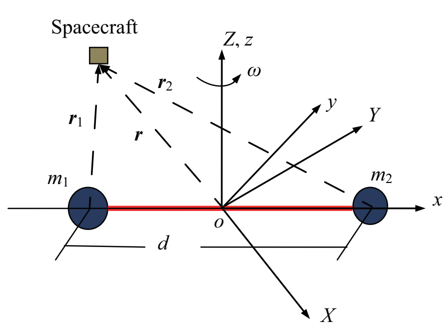

Fig. 1 A schematic diagram of the rotating mass dipole and the coordinate system.

The equation describing uncontrolled motion for a spacecraft relative to a rotating asteroid can be written as follows (Jiang et al. 2014)

$$\ddot{\boldsymbol{r}} + 2\boldsymbol{\omega} \times \dot{\boldsymbol{r}} + \boldsymbol{\omega} \times (\boldsymbol{\omega} \times \boldsymbol{r}) + \dot{\boldsymbol{\omega}} \times \boldsymbol{r} + \frac{\partial U(\boldsymbol{r})}{\partial \boldsymbol{r}} = 0\,, \tag{1}$$

where $\boldsymbol{r}$ is the position vector in the body-fixed frame from the center of mass of the asteroid to the spacecraft and $U(\boldsymbol{r})$ is the gravitational potential. This dynamical equation is established using an assumption that the mass of the spacecraft is negligible compared with the mass of the asteroid. To describe the dynamics of a controlled spacecraft, Equation (1) is modified to be

$$\ddot{\boldsymbol{r}} + 2\boldsymbol{\omega} \times \dot{\boldsymbol{r}} + \boldsymbol{\omega} \times (\boldsymbol{\omega} \times \boldsymbol{r}) + \dot{\boldsymbol{\omega}} \times \boldsymbol{r} + \frac{\partial U(\boldsymbol{r})}{\partial \boldsymbol{r}} = \boldsymbol{a}_c\,, \tag{2}$$

where $\boldsymbol{a}_c$ is the acceleration provided by the low thruster. This acceleration is expressed in the synodic frame. The acceleration in the inertial frame at time t can be easily obtained by $\bar{\boldsymbol{a}}_c(t) = R_z(-\omega t)\,\boldsymbol{a}_c$, where the rotation matrix is

$$R_z(-\omega t) = \begin{bmatrix} \cos(\omega t) & -\sin(\omega t) & 0 \\ \sin(\omega t) & \cos(\omega t) & 0 \\ 0 & 0 & 1 \end{bmatrix}.$$

Assuming that the asteroid rotates uniformly ($\dot{\boldsymbol{\omega}} = 0$), we can define an effective potential as (Yu & Baoyin 2012; Jiang et al. 2014)

$$V(\boldsymbol{r}) = -\frac{1}{2}(\boldsymbol{\omega} \times \boldsymbol{r})(\boldsymbol{\omega} \times \boldsymbol{r}) + U(\boldsymbol{r})\,. \tag{3}$$

Equation (2) can be rewritten as

$$\ddot{\boldsymbol{r}} + 2\boldsymbol{\omega} \times \dot{\boldsymbol{r}} + \frac{\partial V(\boldsymbol{r})}{\partial \boldsymbol{r}} = \boldsymbol{a}_c\,. \tag{4}$$

In the case of the rotating mass dipole, a previous work (Zeng et al. 2014b) has given the normalized dynamical equations as follows. The gravitational potential can be obtained as

$$U(\boldsymbol{r}) = -\frac{Gm_1}{r_1} - \frac{Gm_2}{r_2}\,, \tag{5}$$

where G is the gravitational constant, and r_1 and r_2 are the distances from the spacecraft to the two primaries, respectively. Using normalized units, including mass unit M ($M = m_1 + m_2$), length unit d and time unit ω^{-1}, Equation (4) can be transformed into a normalized form. Denoting the dimensionless mass of the second primary as $\mu = m_2/M \in (0, 0.5]$ and that of the first primary as $1-\mu \in [0.5, 1)$, the position vectors of the two primaries are $[-\mu, 0, 0]^{\mathrm{T}}$ and $[1-\mu, 0, 0]^{\mathrm{T}}$. Then, the distances from the spacecraft to the two primaries are $\boldsymbol{r}_1 = [x+\mu, y, z]^{\mathrm{T}}$ and $\boldsymbol{r}_2 = [x-1+\mu, y, z]^{\mathrm{T}}$.

After normalization, the normalized scalar form of Equation (4) can be obtained

$$\begin{cases} \ddot{x} - 2\dot{y} + \frac{\partial V(x,y,z)}{\partial x} = a_{cx}\,, \\ \ddot{y} + 2\dot{x} + \frac{\partial V(x,y,z)}{\partial y} = a_{cy}\,, \\ \ddot{z} + \frac{\partial V(x,y,z)}{\partial z} = a_{cz}\,, \end{cases} \tag{6}$$

where the effective potential is

$$V = -\frac{x^2 + y^2}{2} - k\left(\frac{1-\mu}{r_1} + \frac{\mu}{r_2}\right). \tag{7}$$

The dimensionless variable k in Equation (7) is equal to $GM/\omega^2 d^3$. The parameter k depends on the physical properties of the asteroid and represents the ratio of the gravitational force to the centrifugal force between the two primaries (Prieto-Llanos & Gomez-Tierno 1994). When k is equal to 1, the dynamical equations are the same as those of the classical CRTBP.

2.2 Condition for Body-fixed Hovering

The velocity and acceleration should be zero in the synodic frame when a spacecraft is performing body-fixed hovering above an asteroid, that is $\ddot{\boldsymbol{r}} = \dot{\boldsymbol{r}} = 0$. Without active control ($a_{cx} = a_{cy} = a_{cz} = 0$), the following condition should be satisfied

$$\frac{\partial V\left(x,y,z\right)}{\partial x} = \frac{\partial V\left(x,y,z\right)}{\partial y} = \frac{\partial V\left(x,y,z\right)}{\partial z} = 0\,. \tag{8}$$

The solutions of Equation (8) are called EPs. When $k = 1$, the solutions of Equation (8) correspond to the five EPs of the CRTBP. For elongated asteroids, there are usually four EPs (one of the other solutions is located in the interior of the asteroid) (Wang et al. 2014). Detailed expressions describing the EPs can be found in the work of Zeng et al. (2014b).

When there is an active control, the body-fixed hovering region can be extended beyond the EPs. The active control should balance the gravitational force and the centrifugal force. The components of the active control should satisfy the following condition:

$$\begin{cases} a_{cx} = \frac{\partial V(x,y,z)}{\partial x}\,, \\ a_{cy} = \frac{\partial V(x,y,z)}{\partial y}\,, \\ a_{cz} = \frac{\partial V(x,y,z)}{\partial z}\,. \end{cases} \tag{9}$$

By substituting Equation (7) into Equation (9), the explicit form of the components required for active control can be obtained:

$$\begin{aligned} a_{cx} &= -x + k\left[\tfrac{1-\mu}{r_1^3}\left(x+\mu\right) + \tfrac{\mu}{r_2^3}\left(x+\mu-1\right)\right], \\ a_{cy} &= -y + k\left[\tfrac{1-\mu}{r_1^3}y + \tfrac{\mu}{r_2^3}y\right], \\ a_{cz} &= k\left[\tfrac{1-\mu}{r_1^3}z + \tfrac{\mu}{r_2^3}z\right]\,. \end{aligned} \tag{10}$$

At a given hovering position, the components needed for active control are constants.

The magnitude of the active control is

$$a_c = \sqrt{a_{cx}^2 + a_{cy}^2 + a_{cz}^2}\,. \tag{11}$$

Because the active control is provided by thrusters mounted on the spacecraft, there is an upper limit on its magnitude

$$a_c \le a_{\max}\,. \tag{12}$$

3 FEASIBLE HOVERING REGION

The feasible hovering region is defined as the region where the gravitational force and the centrifugal force can be balanced by the active control. Hence, the condition described by Equation (12) should be satisfied, otherwise the active control is not able to balance the gravitational force and the centrifugal force. Equation (12) determines the boundary of the feasible hovering region. From Equation (10), it can be found that the components required for active control only depend on two physical parameters, which are μ and k of the asteroid. Therefore, there are only three parameters (μ, k and $a_{\max}$) that completely determine the feasible hovering region. The effects of these three parameters will be analyzed next.

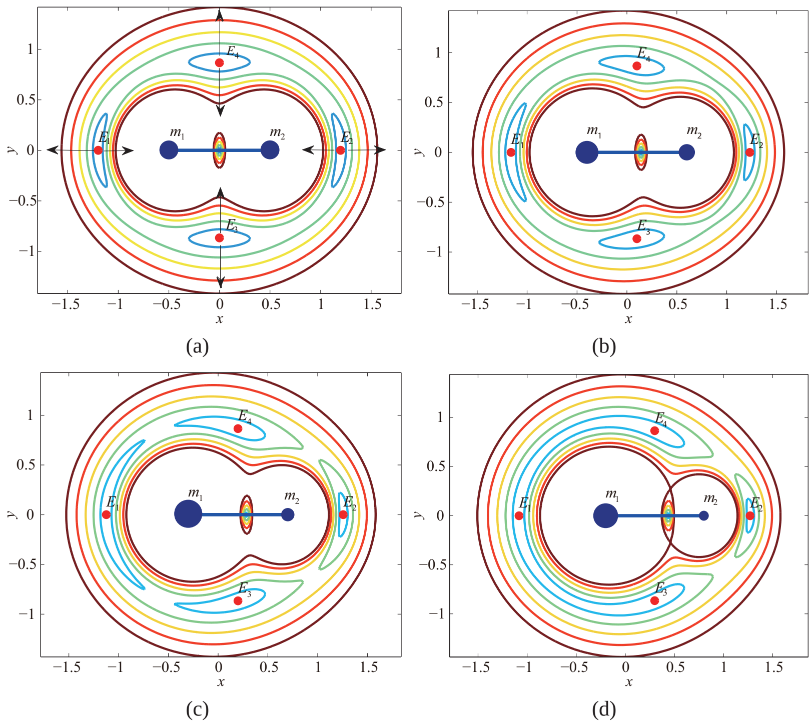

Fig. 2 Contour maps of the active control's magnitude for different μ in the equatorial plane. (a) $\mu = 0.5$ and $k = 1$; (b) $\mu = 0.4$ and $k = 1$; (c) $\mu = 0.3$ and $k = 1$; (d) $\mu = 0.2$ and $k = 1$.

3.1 Equatorial Plane

The body-fixed hovering in the equatorial plane ($z = 0$) will be considered here. From Equation (10), it can be directly obtained that $a_{cz} = 0$. The contour map displaying the magnitude of the required active control can be depicted according to Equation (10) and Equation (11). The contours describe the boundaries of the feasible hovering regions with different magnitudes for active control.

Firstly, setting $\mu = 0.5$ and $k = 1$, the corresponding contour map can be obtained as shown in Figure 2(a). In this figure, the four points named E_i ($i = 1, 2, 3, 4$) denote the four EPs of the dynamical system described by Equation (6) without control, meaning that the magnitude of the active control is zero at these points. The points E_1 and E_2 are called collinear equilibrium points (CEPs). The points E_3 and E_4 are triangular equilibrium points (TEPs). Actually, there is still one more EP which is located inside of the massless rod between the two primaries. However, the position of this EP is in the interior of the asteroid. Hence it is not feasible for hovering. There are some contour lines surround this EP as shown in the figure. The small region where these contour lines locate is considered not feasible as well. These contour lines are all not considered in the analyses below. The normalized values of contour lines have five levels which are 0.2, 0.4, 0.6, 0.8 and 1.0. There are four isolated feasible regions for hovering when $a_{\max} = 0.2$. Each of these regions contains one EP as shown in the figure. When the maximal magnitude of the active control is increased, these regions expand and then become connected to each other. Let us define a parameter

$$dp = \begin{cases} |x - x_{Ei}|, & i = 1, 2 \\ |y - y_{Ei}|, & i = 3, 4 \end{cases}$$

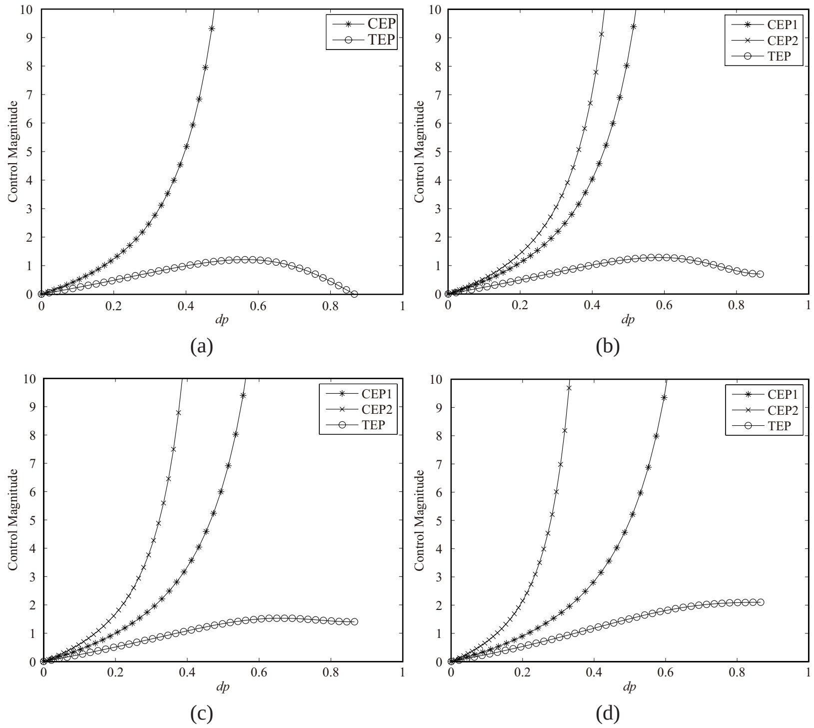

Fig. 3 Magnitude of the required active control as a function of *dp*. (a) $\mu = 0.5$ and $k = 1$; (b) $\mu = 0.4$ and $k = 1$; (c) $\mu = 0.3$ and $k = 1$; (d) $\mu = 0.2$ and $k = 1$.

representing the deviation from an EP towards the asteroid. The relationship of a_c and *dp* is shown in Figure 3. In Figure 3(a), the curve shows a monotone increase and it tends to infinity in the case of deviating from a CEP towards one of the primaries. However, the nominal control required for deviating from a TEP and towards the massless rod is limited and becomes zero again at the massless rod. The contours in Figure 2(a) agree with Figure 3(a). The curves in Figure 3(a) show that close hovering is cheaper in terms of fuel consumption in the vicinity of the middle of an asteroid than in the vicinity of its two ends.

By fixing $k = 1$ and varying μ, Figure 2(b)–(d) is drawn. Two phenomena can be found related to the feasible hovering region that are consequences of the parameter μ decreasing. Firstly, the feasible hovering region close to the first primary stretches while the region close to the second primary shrinks. For $a_{\max} = 0.2$, the region containing E_1 stretches and then becomes connected to the regions containing E_3 and E_4 while the region containing E_2 shrinks with μ decreasing. In addition, the region between E_2 and E_3 or E_4 becomes connected for $a_{\max} = 0.4$ when $\mu = 0.5$. However, this region shrinks and then breaks when μ decreases. Once the contour ($a_{\max} = 0.4$) breaks into two parts, as shown in Figure 2(c)–(d), the two disconnected regions become infeasible for hovering when the maximum magnitude of the nominal control is 0.4. Secondly, the separated exterior contours and interior contours (surrounding the interior EP) can be connected with μ decreasing. This phenomenon appears for $a_{\max} = 1.0$ in the figure. Once the exterior contours and interior contours are connected, the minimum altitude of the feasible region ($a_{\max} = 1.0$) with respect to the asteroid is zero. Hence, a body-fixed hovering which is very close to the surface of the asteroid is possible. Moreover, the magnitudes of the active control with respect to *dp* for μ less than 0.5 can be obtained as shown in Figure 3(b)–(d). The nominal control required for deviating from a TEP does

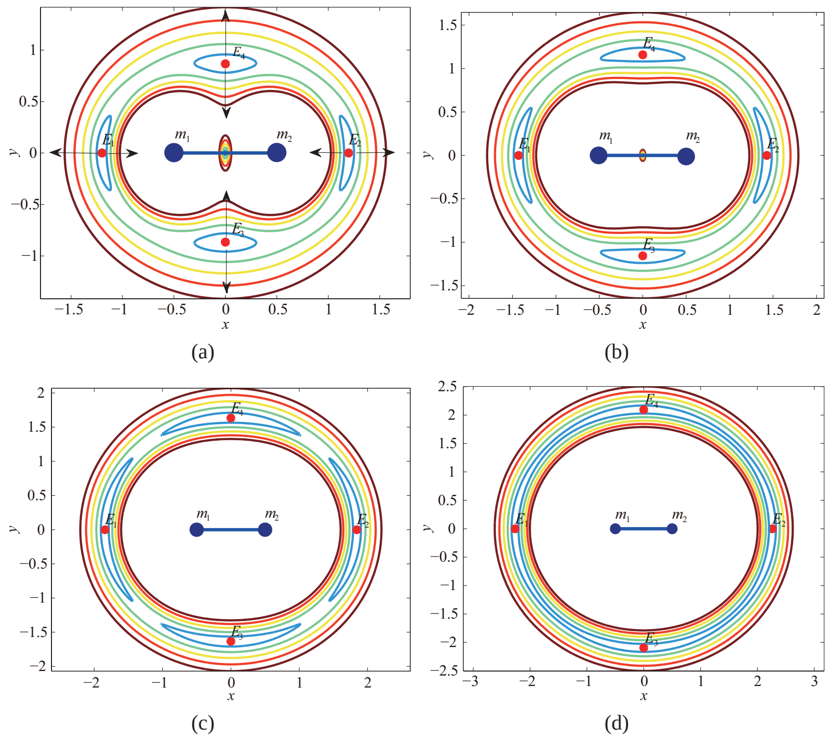

Fig. 4 Contour maps of the magnitude of active control for different k in the equatorial plane. (a) $\mu = 0.5$ and $k = 1$; (b) $\mu = 0.5$ and $k = 2$; (c) $\mu = 0.5$ and $k = 5$; (d) $\mu = 0.5$ and $k = 10$.

not become zero again at the massless rod. This happens because the x coordinate of the interior EP on the massless rod is different from those of the TEPs when μ is not equal to 0.5 as shown in Figure 2(b)–(d). However, the nominal control for a large deviation is still much less than what is required when deviating from a CEP, meaning a close hovering is still cheaper for fuel consumption in the vicinity of the middle of an asteroid. Besides, it can be found by comparing Figure 3(b)–(d) that deviating from the first EP (CEP1) is a little easier than deviating from the second EP (CEP2) in the sense of the required nominal control.

The effect of k is analyzed by fixing $\mu = 0.5$ and varying k. The corresponding contour maps are shown in Figure 4(a)–(d). As for $a_{\max} = 0.2$, the feasible hovering regions are isolated when $k = 1$. With k increasing, these four regions gradually stretch and connect with each other when $k = 10$. For $a_{\max} \geq 0.4$, the inner bounds of the feasible hovering regions gradually tend to be circular and move away from the asteroid with k increasing. Hence, a close hovering requires larger controlled acceleration for a larger k. This phenomenon can be explained simply as follows. From the definition of the dimensionless parameter k, this type of behavior can be regarded as changes in the ratio between the two-body gravitational force and the centrifugal force at the distance d. With k increasing, the distance from the EPs to the center of mass of the asteroid should be larger so that the centrifugal force can balance the gravitational force. Because the feasible hovering regions are surrounding the equilibrium points, these regions also move away from the asteroid. In addition, the irregularity of the gravitational field would be lower with a larger distance to the asteroid. Therefore, the inner bounds of the feasible hovering regions would tend to be circular.

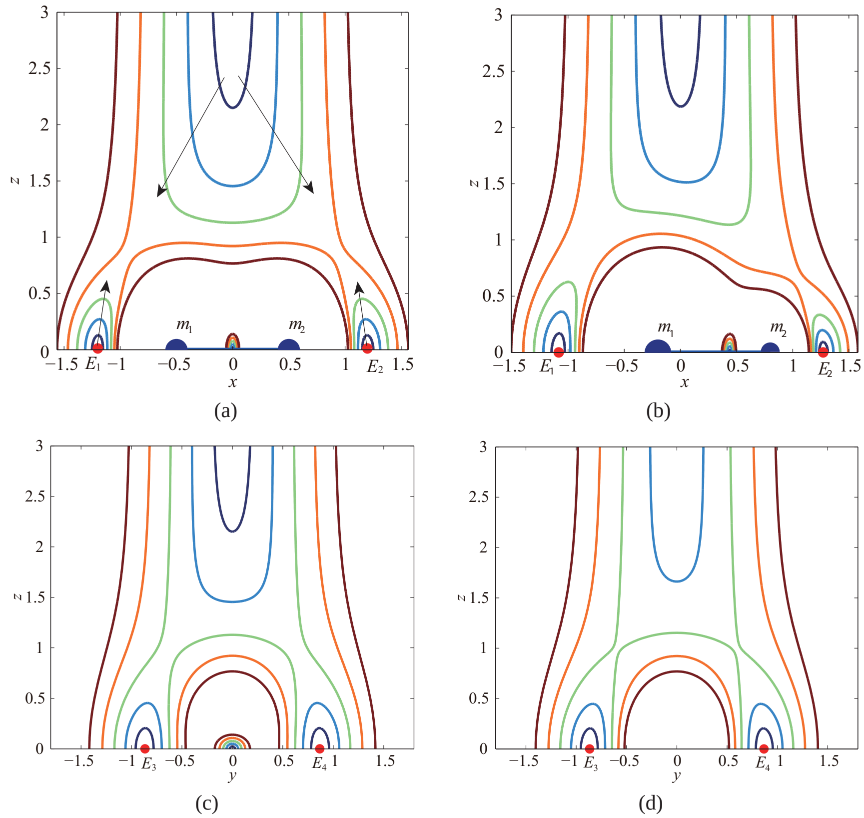

Fig. 5 Contour maps of the magnitude of active control for different μ in the plane E_1E_2 and the plane E_3E_4. (a) $\mu = 0.5$ and $k = 1$ in the plane E_1E_2; (b) $\mu = 0.2$ and $k = 1$ in the plane E_1E_2; (c) $\mu = 0.5$ and $k = 1$ in the plane E_3E_4; (d) $\mu = 0.2$ and $k = 1$ in the plane E_3E_4.

3.2 Out of the Equatorial Plane

Two special planes which are perpendicular to the equatorial plane are considered here. We denote these planes containing E_1, E_2 and E_3, E_4 as plane E_1E_2 and plane E_3E_4, respectively. In view of the symmetry of these planes, only semi-planes will be analyzed. The contour maps for different μ in these two planes are illustrated in Figure 5. The values of contour lines still have five levels which are 0.2, 0.4, 0.6, 0.8 and 1.0. The magnitude of the required active control also increases along the directions of the arrows. The contour lines in the vicinity of the fictitious interior equilibrium point should also be ignored. The feasible hovering regions can be classified into two types: the first surrounds an equilibrium point and the second is over the north pole of the asteroid. These two types of regions are isolated when the maximal magnitude of the active control is small (e.g. $a_{\max} = 0.2$). With the maximal magnitude of active control increasing, these regions stretch toward each other and then become connected. The effect of μ decreasing on feasible hovering regions is found as follows. In the plane E_1E_2, the feasible regions near E_1 become larger than the feasible regions near E_2 while the distance from the inner bounds to the first primary becomes further than the distance from the inner bounds to the second primary when μ is less than 0.5. In the plane E_3E_4, the feasible regions near E_1 and E_4 remain the same due to symmetry when μ is less than 0.5. However, the feasible regions at both sides shrink. The reason for this is as follows. The rotation axis moves out of the plane E_3E_4 when μ is not equal to 0.5, leading the centrifugal force to increase. Hence, the required magnitude of the active control increases at the same position with μ decreasing.

3.3 Actual Magnitude of the Active Control for Elongated Asteroids

The magnitudes of the active control corresponding to the contour lines in Figures 2, 4 and 5 are normalized values. With specified ω and d, the actual magnitudes of the active control can be obtained by multiplying ωd^2. A method for connecting the approximate model with natural elongated bodies has been proposed by Zeng et al. (2014b). We list the resulting parameters of the approximate model for sample natural elongated bodies in Table 1.

Table 1 Parameters of the Approximate Model for Sample Natural Elongated Bodies (Zeng et al. 2014b, Appendix)

Elongated bodies	μ	k	T (h)	M (kg)	d (km)
(216) Kleopatra	0.486298	0.883478	5.385	2.588233E+18	122.9967
(951) Gaspra	0.2496003	5.3814122	7.042	2.31959126E+15	7.7649056
(1620) Geographos	0.440043	1.158476	5.223	2.1644546E+13	2.234946
(1996) HW1	0.41255886	3.8663816	8.757	1.5625969E+13	1.8934394
(2063) Bacchus	0.4445476	13.049195	14.9	2.7244747E+11	0.46650643
(25143) Itokawa	0.43473655	15.655407	12.132	4.7313275E+10	0.2135805

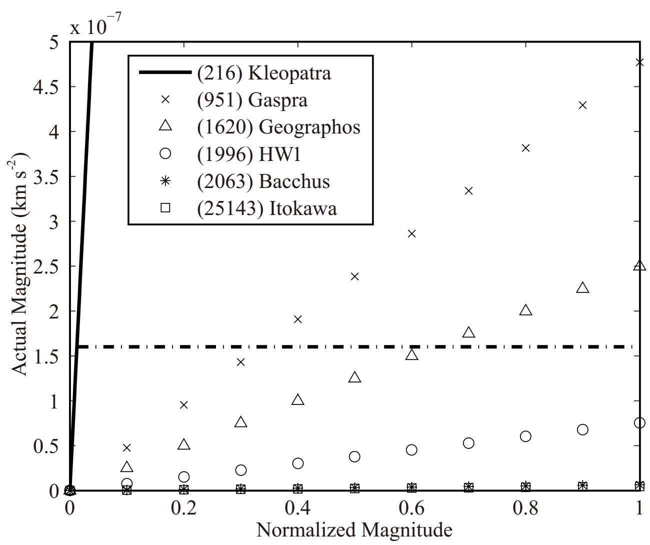

Fig. 6 Actual magnitude with respect to normalized magnitude of the active control for different asteroids.

Using these parameters, the actual magnitudes of the active control for different asteroids are obtained as shown in Figure 6. The dot dashed line in this figure represents the maximal acceleration which can be provided by two 0.08 N low thrusters acting on a 1000 kg spacecraft. Assuming the spacecraft is equipped with these low thrusters, then the actual magnitude of the active control should be less than the maximal acceleration provided by these low thrusters. For asteroids with small sizes

((1996) HW1, (2063) Bacchus and (25143) Itokawa), the magnitude of the normalized active control that can be provided by the low thrusters can be much larger than 1.0, as shown in Figure 6. Hence, it is possible to execute body-fixed hovering around these asteroids by applying low thrust.

4 ANALYSIS OF HOVERING STABILITY

Because there are perturbations in the vicinity of asteroids, the stability of body-fixed hovering is addressed here. The effect of μ and k on hovering stability will be analyzed.

4.1 Linearization near the Hovering Position

Denote the hovering position as $\boldsymbol{r}_0 = [x_0, y_0, z_0]^{\mathrm{T}}$ and consider a small perturbation $\delta\boldsymbol{r} = [\xi, \eta, \zeta]^{\mathrm{T}}$. The equations describing the dynamics near the hovering position can then be derived from Equation (6):

$$\begin{aligned}
&\ddot{\xi} - 2\dot{\eta} + \tfrac{\partial V(\boldsymbol{r}_0+\delta\boldsymbol{r})}{\partial x} = a_{cx}\left(\boldsymbol{r}_0 + \delta\boldsymbol{r}\right) \,, \\
&\ddot{\eta} + 2\dot{\xi} + \tfrac{\partial V(\boldsymbol{r}_0+\delta\boldsymbol{r})}{\partial y} = a_{cy}\left(\boldsymbol{r}_0 + \delta\boldsymbol{r}\right) \,, \\
&\ddot{\zeta} + \tfrac{\partial V(\boldsymbol{r}_0+\delta\boldsymbol{r})}{\partial z} = a_{cz}\left(\boldsymbol{r}_0 + \delta\boldsymbol{r}\right) \,.
\end{aligned} \tag{13}$$

The gradient of the effective potential and the control acceleration can be expressed as Taylor expansions:

$$\frac{\partial V\left(\boldsymbol{r}_0 + \delta\boldsymbol{r}\right)}{\partial\boldsymbol{r}} = \frac{\partial V\left(\boldsymbol{r}_0\right)}{\partial\boldsymbol{r}} + \frac{\partial^2 V\left(\boldsymbol{r}_0\right)}{\partial\boldsymbol{r}^2}\delta\boldsymbol{r} + O\left(\delta\boldsymbol{r}^2\right), \tag{14}$$

$$\boldsymbol{a}_c\left(\boldsymbol{r}_0 + \delta\boldsymbol{r}\right) = \boldsymbol{a}_c\left(\boldsymbol{r}_0\right) + \frac{\partial\boldsymbol{a}_c\left(\boldsymbol{r}_0\right)}{\partial\boldsymbol{r}}\delta\boldsymbol{r} + O\left(\delta\boldsymbol{r}^2\right). \tag{15}$$

Because the active control is constant at a given hovering position, it can be obtained that

$$\frac{\partial\boldsymbol{a}_c\left(\boldsymbol{r}_0\right)}{\partial\mathbf{r}} = 0\,. \tag{16}$$

Denote the Hessian matrix as

$$\frac{\partial^2 V\left(\boldsymbol{r}\right)}{\partial\boldsymbol{r}^2} = \begin{bmatrix} V_{xx} & V_{xy} & V_{xz} \\ V_{yx} & V_{yy} & V_{yz} \\ V_{zx} & V_{zy} & V_{zz} \end{bmatrix} . \tag{17}$$

The elements in this matrix are

$$\begin{aligned}
&V_{xx} = -1 + k\left[\tfrac{1-\mu}{r_1^3} - 3\tfrac{(1-\mu)(x+\mu)^2}{r_1^5} + \tfrac{\mu}{r_2^3} - 3\tfrac{\mu(x-1+\mu)^2}{r_2^5}\right] \,, \\
&V_{yy} = -1 + k\left[\tfrac{1-\mu}{r_1^3} - 3\tfrac{(1-\mu)y^2}{r_1^5} + \tfrac{\mu}{r_2^3} - 3\tfrac{\mu y^2}{r_2^5}\right] \,, \\
&V_{zz} = k\left[\tfrac{1-\mu}{r_1^3} - 3\tfrac{(1-\mu)z^2}{r_1^5} + \tfrac{\mu}{r_2^3} - 3\tfrac{\mu z^2}{r_2^5}\right] \,, \\
&V_{xy} = V_{yx} = -3ky\left[\tfrac{(1-\mu)(x+\mu)}{r_1^5} + \tfrac{\mu(x-1+\mu)}{r_2^5}\right] \,, \\
&V_{xz} = V_{zx} = -3kz\left[\tfrac{(1-\mu)(x+\mu)}{r_1^5} + \tfrac{\mu(x-1+\mu)}{r_2^5}\right] \,, \\
&V_{yz} = V_{zy} = -3kyz\left[\tfrac{1-\mu}{r_1^5} + \tfrac{\mu}{r_2^5}\right] \,.
\end{aligned} \tag{18}$$

By substituting Equation (14) into Equation (13) and using the relationship that

$$\frac{\partial V\left(\boldsymbol{r}_0\right)}{\partial\boldsymbol{r}} = \boldsymbol{a}_c\left(\boldsymbol{r}_0\right), \tag{19}$$

the scalar linearized equations near the hovering position can be derived:

$$
\begin{aligned}
&\ddot{\xi}-2\dot{\eta}+V_{xx}\left(\boldsymbol{r}_0\right)\xi+V_{xy}\left(\boldsymbol{r}_0\right)\eta+V_{xz}\left(\boldsymbol{r}_0\right)\zeta=0\,,\\
&\ddot{\eta}+2\dot{\xi}+V_{xy}\left(\boldsymbol{r}_0\right)\xi+V_{yy}\left(\boldsymbol{r}_0\right)\eta+V_{yz}\left(\boldsymbol{r}_0\right)\zeta=0\,,\\
&\ddot{\zeta}+V_{xz}\left(\boldsymbol{r}_0\right)\xi+V_{yz}\left(\boldsymbol{r}_0\right)\eta+V_{zz}\left(\boldsymbol{r}_0\right)\zeta=0\,.
\end{aligned}
\tag{20}
$$

4.2 Stability Conditions

The characteristic equation of Equation (20) is

$$
\begin{vmatrix}
\lambda^2+V_{xx}\left(\boldsymbol{r}_0\right) & -2\lambda+V_{xy}\left(\boldsymbol{r}_0\right) & V_{xz}\left(\boldsymbol{r}_0\right)\\
2\lambda+V_{xy}\left(\boldsymbol{r}_0\right) & \lambda^2+V_{yy}\left(\boldsymbol{r}_0\right) & V_{yz}\left(\boldsymbol{r}_0\right)\\
V_{xz}\left(\boldsymbol{r}_0\right) & V_{yz}\left(\boldsymbol{r}_0\right) & \lambda^2+V_{zz}\left(\boldsymbol{r}_0\right)
\end{vmatrix}=0\,,
\tag{21}
$$

where λ denotes the eigenvalues of Equation (20). Equation (21) can be expanded to be

$$
\begin{aligned}
\lambda^6 \quad &+\left(V_{xx}+V_{yy}+V_{zz}+4\right)_{\boldsymbol{r}=\boldsymbol{r}_0}\lambda^4\\
&+\left(V_{xx}V_{yy}+V_{yy}V_{zz}+V_{zz}V_{xx}-V_{xy}^2-V_{yz}^2-V_{xz}^2+4V_{zz}\right)_{\boldsymbol{r}=\boldsymbol{r}_0}\lambda^2\\
&+\left(V_{xx}V_{yy}V_{zz}+2V_{xy}V_{yz}V_{xz}-V_{xx}V_{yz}^2-V_{yy}V_{xz}^2-V_{zz}V_{xy}^2\right)_{\boldsymbol{r}=\boldsymbol{r}_0}=0\,.
\end{aligned}
\tag{22}
$$

The eigenvalues of Equation (22) determine the stability of the linearized system described by Equation (20). Because the form of the characteristic equation is the same as that in the work of Jiang et al. (2014), the possible forms of the eigenvalues should be the same. The possible forms of the eigenvalues at non-degenerate equilibriums are $\pm\alpha\,(\alpha\in R,\alpha>0)$, $\pm i\beta\,(\beta\in R,\beta>0)$, and $\pm\sigma\pm i\tau\,(\sigma,\tau\in R;\sigma,\tau>0)$ (Jiang et al. 2014). An additional form of the eigenvalues can be zero. If a system is stable, all of the real parts of the eigenvalues should be no larger than zero. The derivation of the stability conditions is similar to the work of Morimoto et al. (2007) in which the stability conditions for the AEPs in the CRTBP are as follows. Denoting $s=\lambda^2$, Equation (22) can be written as

$$
s^3+Ps^2+Qs+R=0\,,
\tag{23}
$$

where

$$
\begin{aligned}
P&=\left(V_{xx}+V_{yy}+V_{zz}+4\right)_{\boldsymbol{r}=\boldsymbol{r}_0}\equiv 2\,,\\
Q&=\left(V_{xx}V_{yy}+V_{yy}V_{zz}+V_{zz}V_{xx}-V_{xy}^2-V_{yz}^2-V_{xz}^2+4V_{zz}\right)_{\boldsymbol{r}=\boldsymbol{r}_0}\,,\\
R&=\left(V_{xx}V_{yy}V_{zz}+2V_{xy}V_{yz}V_{xz}-V_{xx}V_{yz}^2-V_{yy}V_{xz}^2-V_{zz}V_{xy}^2\right)_{\boldsymbol{r}=\boldsymbol{r}_0}\,.
\end{aligned}
\tag{24}
$$

Because P is never equal to zero, the solutions of the cubic equation cannot all be zeros. Hence, the eigenvalues are either all imaginary numbers or imaginary numbers and zeros. Then, the corresponding motion around the hovering point will be oscillating. If all of the eigenvalues are imaginary numbers or zeros, then the solution s of the cubic equation above should be negative numbers or zeros. The resulting stability conditions are

$$
\Delta\le 0,\ Q\ge 0,\ R\ge 0\,,
\tag{25}
$$

where Δ is the discriminant of the cubic equation and is defined as

$$
\Delta=\left(\frac{q}{2}\right)^2+\left(\frac{p}{3}\right)^3,
\tag{26}
$$

where

$$
\begin{aligned}
p&=Q-\tfrac{P^2}{3}\,,\\
q&=\tfrac{2P^3}{27}-\tfrac{PQ}{3}+R\,.
\end{aligned}
$$

The first condition in Equation (25) is necessary and sufficient for all solutions of the cubic equation to be real numbers. Combined with the last two conditions in Equation (25), these conditions are necessary and sufficient for all solutions to be not positive according to Descartes' rule of signs. Hence, the regions where stable hovering can occur are determined by Equation (25). It should be noted that linear stability is a necessary condition for nonlinear stability and linear instability is a sufficient condition for nonlinear instability. Hence, the stable regions found by Equation (25) can only be guaranteed to be linearly stable instead of nonlinearly stable.

4.3 Analysis of Stable Regions

Stable regions in the three special planes, including the equatorial plane, the plane E_1E_2 and the plane E_3E_4, are analyzed here. A two dimensional grid search method is used to determine the stable regions. The normalized searching steps in the two dimensions are both 0.01. The stable regions for different μ and k in these planes are depicted in Figures 7–9.

In the equatorial plane, there are two separated narrow stable regions surrounding the point E_1 and the point E_2 when $\mu = 0.5$ and $k = 1$. The stable region close to point E_1 becomes larger than the stable region close to point E_2 as μ becomes less than 0.5 (e.g. $\mu = 0.2$). These two separated regions can become connected as k increases, as shown in Figure 7(c) and (d). From Figure 7(c) and (d), it can be seen that the CEPs are inside the stable region while the TEPs are outside this region. A closer and stable hovering point separate from the TEPs is feasible using low thrust for the asteroid with a large k in the equatorial plane. Moreover, the stable regions tend to be circular as k increases, as shown in the figure.

In the plane E_1E_2, there are two types of stable regions. The first kind of stable region contains four separated regions far from the CEPs and the second kind contains two regions beyond the two CEPs as shown in the figure. Comparing the first two situations in Figure 8, it can be found that the second kind of stable region becomes a little closer to point E_1 than point E_2 with μ decreasing. Moreover, both types of stable regions move away from the asteroid for larger k, as can be seen by comparing Figure 8(a), (c) and (d). Moreover, the two small stable regions close to the equilibrium points become larger when k increases.

In the plane E_3E_4, there are four stable regions when $\mu = 0.5$ and $k = 1$. There is one end in each region whose distance to the asteroid is closer than the two TEPs. These end regions will move away from the asteroid and become wide with μ decreasing, as shown in Figure 9(b). Keeping $\mu = 0.5$ and increasing k up to ten, the two stable regions on both sides (left and right) shrink and break into two parts, as shown in Figure 9(d), (e) and (f). The main part of each original stable region stretches to become connected with each other. The connected regions are still closer to the asteroid than the two TEPs. Moreover, four small and isolated stable regions (the small parts of each original stable region) are close to the asteroid and suitable for hovering. The size of these four regions decreases with k increasing, as shown in Figure 9(d), (e) and (f).

From Figure 7 to Figure 9, the stable regions move away from the asteroid with k increasing. Moreover, it can be found that the stable regions in the vicinity of ends of the asteroid are beyond the CEPs while the stable regions in the vicinity of the middle of the asteroid can be closer to the asteroid than the TEPs. Hence, a close hovering is easier in the vicinity of the middle side of asteroid in the sense of the stability.

5 CONCLUSIONS

A normalized rotating mass dipole model has been used to analyze the feasible region and stability for body-fixed hovering around elongated asteroids in which the rotating gravitational field is described by two independent parameters, μ and k. The perturbations from the Sun and other planets are ignored in this study. The boundaries of the feasible hovering regions with respect to different

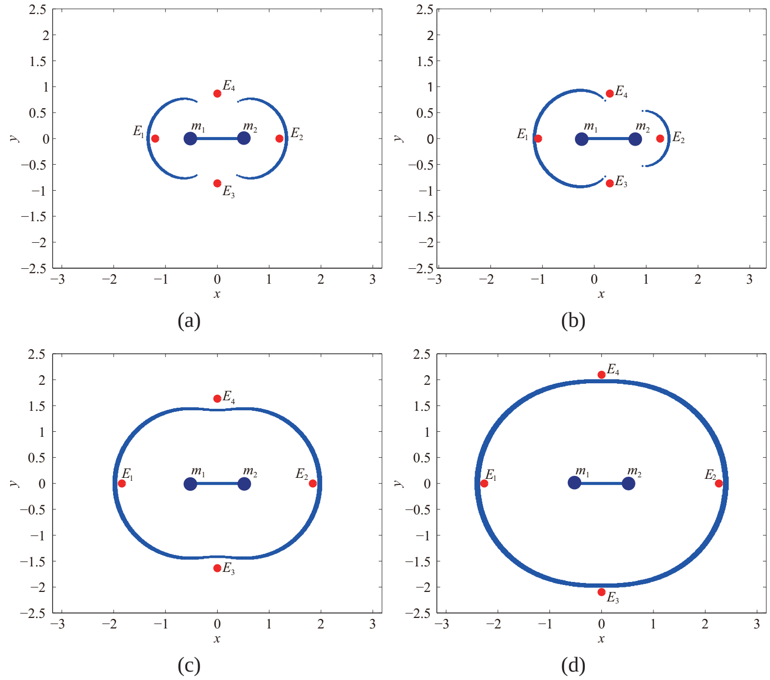

Fig. 7 Stable regions in the equatorial plane for different μ and k. (a) $\mu = 0.5$ and $k = 1$; (b) $\mu = 0.2$ and $k = 1$; (c) $\mu = 0.5$ and $k = 5$; (d) $\mu = 0.5$ and $k = 10$.

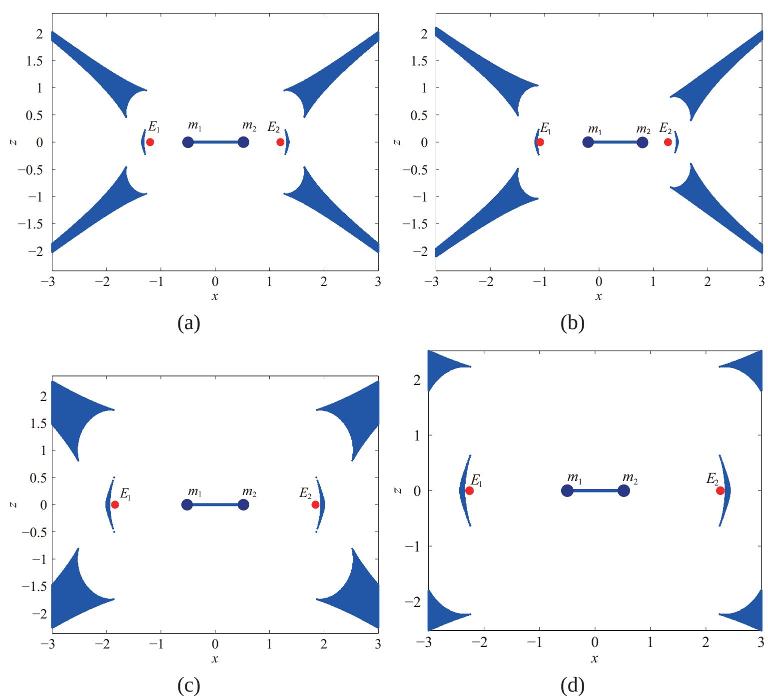

Fig. 8 Stable regions in the plane E_1E_2 for different μ and k. (a) $\mu = 0.5$ and $k = 1$; (b) $\mu = 0.2$ and $k = 1$; (c) $\mu = 0.5$ and $k = 5$; (d) $\mu = 0.5$ and $k = 10$.

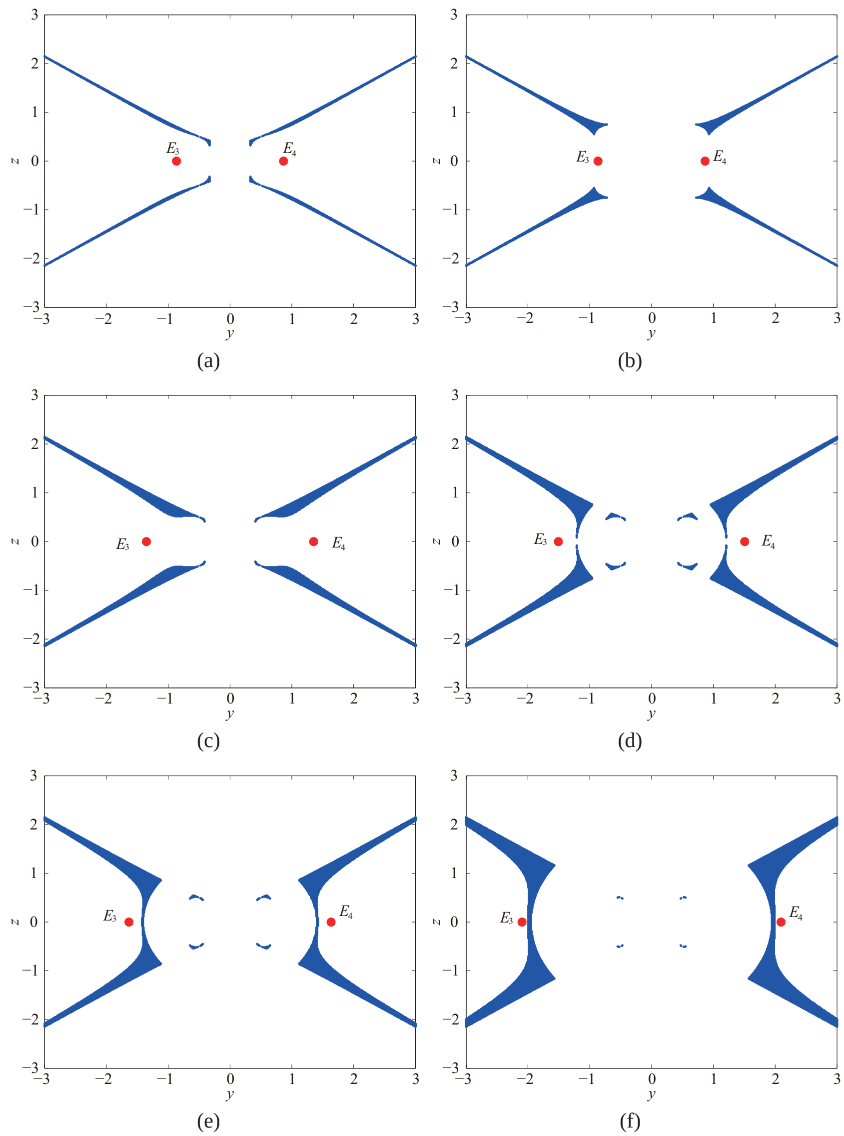

Fig. 9 Stable regions in the plane E_3E_4 for different μ and k. (a) $\mu = 0.5$ and $k = 1$; (b) $\mu = 0.2$ and $k = 1$; (c) $\mu = 0.5$ and $k = 3$; (d) $\mu = 0.5$ and $k = 4$; (e) $\mu = 0.5$ and $k = 5$; (f) $\mu = 0.5$ and $k = 10$.

maximal magnitudes that are necessary for active control are determined by the contour maps. The effects of the parameters μ and k on the feasible hovering region have been analyzed individually by comparing the contour maps. The feasible region near the equilibrium point E_1 becomes larger than the one near the equilibrium point E_2 when μ decreases below 0.5. The contour lines can also become connected to the massless rod when μ decreases, making close hovering near the middle of the asteroid easier in the sense of the magnitude required for active control. The contour lines move away from the asteroid surface by increasing k, resulting in hovering close to the asteroid being more difficult. For small size asteroids (such as (1996) HW1, (2063) Bacchus and (25143) Itokawa), body-fixed hovering is possible using low thrust. The stability conditions for body-fixed hovering have been derived and the corresponding stable regions are determined by a two dimensional grid search. The effect of k is more significant than μ on stable regions. The number of stable regions both in the equatorial plane and the plane E_3E_4 changes with k increasing, and the stable regions also move away from the asteroid. Moreover, it is found that close hovering is easier in the vicinity of the middle side of the asteroid than the two ends in the sense of the stability.

Acknowledgements This work is supported by the National Natural Science Foundation of China (No. 11372150) and the National Basic Research Program of China (973 Program, 2012CB720000).

References

Baig, S., & McInnes, C. 2008, Journal of Guidance Control Dynamics, 31, 1644
Baoyin, H., & McInnes, C. R. 2006, Celestial Mechanics and Dynamical Astronomy, 94, 155
Bartczak, P., & Breiter, S. 2003, Celestial Mechanics and Dynamical Astronomy, 86, 131
Barucci, M. A., Cheng, A. F., Michel, P., et al. 2012, Experimental Astronomy, 33, 645
Broschart, S. B., & Scheeres, D. J. 2005, Journal of Guidance Control Dynamics, 28, 343
Dunham, D. W., Farquhar, R. W., McAdams, J. V., et al. 2002, Icarus, 159, 433
Gaudet, B., & Furfaro, R. 2012, in AIAA/AAS Astrodynamics Specialist Conference, AIAA 2012-5072
Huang, J., Ji, J., Ye, P. et al., 2013, Scientific Report, 3, *http://www.nature.com/srep/2013/131212/srep03411/full/srep03411.html?WT.ec_id=SREP-704-20140102*
Ji, J.-H., & Liu, L. 2007, ChJAA (Chin. J. Astron. Astrophys.), 7, 148
Jiang, Y., Baoyin, H., Li, J., & Li, H. 2014, Ap&SS, 349, 83
Kawaguchi, J., Fujiwara, A., & Uesugi, T. 2008, Acta Astronautica, 62, 639
Kuninaka, H., Nishiyama, K., Funaki, I., et al. 2007, Journal of Propulsion and Power, 23, 544
Lauretta, D. S., & OSIRIS-Rex Team 2012, in Lunar and Planetary Science Conference, 43, 2491
Llanos, P. J., Jordán, J. D., Hintz, G. R., & Sanjurjo-Rivo, M. 2014, in AIAA/AAS Space Flight Mechanics Meeting, 360, 1
Morimoto, M. Y., Yamakawa, H., & Uesugi, K. 2007, Journal of Guidance Control Dynamics, 30, 1563
Prieto-Llanos, T., & Gomez-Tierno, M. A. 1994, Journal of Guidance Control Dynamics, 17, 787
Riaguas, A., Elipe, A., & Lara, M. 1999, Celestial Mechanics and Dynamical Astronomy, 73, 169
Russell, C. T., & Raymond, C. A. 2012, in The Dawn Mission to Minor Planets 4 Vesta and 1 Ceres (Springer), 3
Sawai, S., Scheeres, D. J., & Broschart, S. B. 2002, Journal of Guidance Control Dynamics, 25, 786
Scheeres, D. 2004, in Planetary Defense Conference: Protecting Earth from Asteroids, Orange County, CA, AIAA, 1445
Scheeres, D. J. 2012, Journal of Guidance, Control, and Dynamics, 35, 987
Scheeres, D. J., Williams, B. G., & Miller, J. K. 2000, Journal of Guidance Control Dynamics, 23, 466
Tsuda, Y., Yoshikawa, M., Abe, M., Minamino, H., & Nakazawa, S. 2013, Acta Astronautica, 91, 356
Wang, X., Jiang, Y., & Gong, S. 2014, Ap&SS, 353, 105
Werner, R. A., & Scheeres, D. J. 1996, Celestial Mechanics and Dynamical Astronomy, 65, 313
Williams, T., & Abate, M. 2009, Journal of Spacecraft and Rockets, 46, 967
Yu, Y., & Baoyin, H. 2012, AJ, 143, 62
Zeng, X.-Y., Jiang, F.-H., & Li, J.-F. 2014a, arXiv:1407.6962
Zeng, X., Jiang, F., Li, J., & Baoyin, H. 2014b, Ap&SS(10.1007/s10509-014-2187-1)